

## A BJT-Based Temperature-to-Digital Converter With a 0.25 C $\pm 3\%$ -Inaccuracy From -40 C to 180 C Using Heater-Assisted Voltage Calibration

Yousefzadeh, Bahman; Makinwa, Kofi A.A.

**DOI**

[10.1109/JSSC.2019.2953834](https://doi.org/10.1109/JSSC.2019.2953834)

**Publication date**

2020

**Document Version**

Accepted author manuscript

**Published in**

IEEE Journal of Solid-State Circuits

**Citation (APA)**

Yousefzadeh, B., & Makinwa, K. A. A. (2020). A BJT-Based Temperature-to-Digital Converter With a 0.25 C  $\pm 3\%$  -Inaccuracy From -40 C to 180 C Using Heater-Assisted Voltage Calibration. *IEEE Journal of Solid-State Circuits*, 55(2), 369-377. Article 8920095. <https://doi.org/10.1109/JSSC.2019.2953834>

**Important note**

To cite this publication, please use the final published version (if applicable). Please check the document version above.

**Copyright**

Other than for strictly personal use, it is not permitted to download, forward or distribute the text or part of it, without the consent of the author(s) and/or copyright holder(s), unless the work is under an open content license such as Creative Commons.

**Takedown policy**

Please contact us and provide details if you believe this document breaches copyrights. We will remove access to the work immediately and investigate your claim.

# A BJT-based Temperature-to-Digital Converter with a $\pm 0.25^\circ\text{C}$ $3\sigma$ -Inaccuracy from $-40^\circ\text{C}$ to $+180^\circ\text{C}$ Using Heater-Assisted Voltage Calibration

Bahman Yousefzadeh, *Member, IEEE*, and Kofi A. A. Makinwa, *Fellow, IEEE*

**Abstract**—This paper presents a BJT-based Temperature-to-Digital-Converter (TDC) that achieves  $\pm 0.25^\circ\text{C}$   $3\sigma$ -inaccuracy from  $-40^\circ\text{C}$  to  $+180^\circ\text{C}$  after a heater assisted voltage calibration. Its switched-capacitor (SC) ADC employs two sampling-capacitors, and thus the minimum number of critical sampling switches, which minimizes the effects of switch leakage at high temperatures and improves accuracy. The TDC is also equipped with an on-chip heater, with which the sensing BJTs can be rapidly ( $< 0.5$  s) heated to about  $110^\circ\text{C}$ . This, in turn, enables voltage calibration at two different temperatures without the need for a temperature-controlled environment. Realized in a  $0.16\ \mu\text{m}$  standard CMOS, the TDC, including the on-chip heater, occupies  $0.15\ \text{mm}^2$  and operates from  $1.8\ \text{V}$ .

**Index Terms**—BJT, Calibration, Heater-assisted, Low leakage, On-chip heater, Temperature sensor, Voltage calibration.

## I. INTRODUCTION

ACCURATE temperature sensing at high temperatures ( $> 150^\circ\text{C}$ ) is often required in automotive applications, for instance in engine or transmission control, or the measurement and control of air, gases, and fluids [1], [2]. In such applications, BJT-based sensors are the preferred choice due to their well-known behavior, long-term stability and high accuracy after a 1-point calibration [3]–[7].

At high temperatures, however, exponentially increasing leakage currents can significantly alter the bias currents of the sensing BJTs, leading to temperature-sensing errors. To mitigate such errors, BJT-based sensors have either employed relatively large biasing currents [3], been realized in low-leakage SOI processes [4], [5], or have employed leakage compensation schemes [6], [7]. Good accuracy at high temperatures is thus achieved at the expense of higher power consumption, complexity, or cost.

Thermal diffusivity (TD) sensors [8], and resistor-based sensors [9] have also demonstrated good accuracy at high temperatures. Compared to BJT-based sensors, however, the milliwatt-level power dissipation of TD sensors, and the 2-point calibration required by precision resistor-based TDCs makes them less suitable for automotive applications.

Another drawback of BJT-based temperature sensors is their stress dependency, which increases their inaccuracy after

plastic packaging [10], [11]. This then necessitates 1- or 2-point post-packaging calibration, which is significantly more expensive than wafer-level calibration.

In this work, a precision BJT-based Temperature-to-Digital-Converter (TDC) is proposed that can operate up to  $180^\circ\text{C}$  without the aforementioned drawbacks. It employs a switched capacitor (SC) ADC to sample and digitize the base-emitter voltages of two sensing BJTs. The ADC employs two sampling capacitors and thus the minimum number of sampling switches, which mitigates the effect of switch leakage at high temperatures. As a result, the sensing BJTs can be biased at low current levels, while still obtaining state-of-the-art inaccuracy and power consumption.

The proposed TDC is also equipped with an on-chip heater, with which the sensing BJTs can be rapidly heated. This facilitates a rapid 2-point calibration without the need for a temperature-controlled environment. This low-cost Heater-Assisted Voltage Calibration (HA-VCAL) can be carried out after plastic packaging to correct for stress-related shifts [10].

The paper is organized as follows. Section II describes the TDC's front-end, and provides some background about both conventional temperature and voltage calibration methods. Section III then elaborates on the proposed heater-assisted voltage calibration scheme, the realization of the on-chip heater, and potential error sources. Section IV provides a leakage analysis and presents a detailed description of the operation of the SC-ADC. Section V includes experimental results, and finally, section VI concludes the paper.

## II. BACKGROUND

### A. Sensing front-end

Fig. 1 shows the front-end of the TDC, which consists of a bipolar core and a bias circuit. As in [10], the bipolar core generates temperature-dependent voltages  $V_{BE}$  ( $= V_{BE2}$ ), and  $\Delta V_{BE}$  ( $= V_{BE2} - V_{BE1}$ ) from two PNPs ( $Q_L$ , and  $Q_R$ ), which are biased at a current density ratio of  $1 : 5$ . The required bias currents are generated by the bias circuit with the help of another pair of PNPs ( $Q_{Lb}$ , and  $Q_{Rb}$ ), which are also biased at a  $1 : 5$  current density ratio. An opamp forces the resulting  $\Delta V_{BEb}$  across a poly resistor  $R_b$ , thus generating a Proportional-to-Absolute-Temperature (PTAT) bias current  $I_b$  ( $= \Delta V_{BEb}/R_b$ ). A second poly-resistor,  $R_\beta$  ( $= R_b/5$ ) cancels the effect of  $\beta$  on  $V_{BE}$  by making  $I_b$  slightly  $\beta$ -dependent [12], [13].

B. Yousefzadeh was with the Department of Microelectronics, Delft University of Technology, 2628CD, Delft, The Netherlands. He is now with NXP Semiconductors, 5656AE, Eindhoven, The Netherlands. (e-mail:bahman.yousefzadeh@gmail.com)

K. A. A. Makinwa is with the Department of Microelectronics, Delft University of Technology, 2628CD, Delft, The Netherlands.

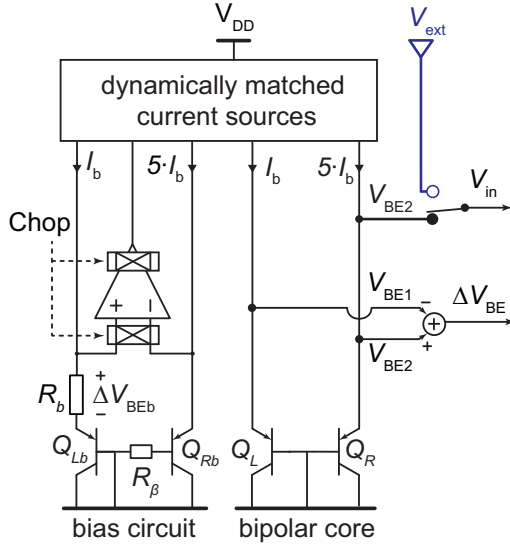


Fig. 1. Sensor front-end, which generates  $V_{BE1}$ ,  $V_{BE2}$  and  $\Delta V_{BE}$ . During Voltage calibration,  $V_{BE2}$  is replaced by an external reference  $V_{ext}$ .

The opamp employs a folded-cascode topology, which achieves more than 90 dB DC-gain over process and temperature variations. Its offset is mitigated by chopping, while dynamic element matching (DEM) ensures accurate 1 : 5 ratios in both the bias circuit and the bipolar core [14].

### B. Temperature calibration

The front-end is followed by an ADC which digitizes the temperature-dependent ratio  $X_T = V_{BE}/\Delta V_{BE}$ , where  $X_T$  is a non-linear function of temperature. A linear function of temperature can then be obtained in the digital domain by computing  $\mu_T = \alpha/(\alpha + X_T)$ , where  $\alpha$  ( $\sim 16$ ) is a calibration parameter [13-14]. This can then be mapped to degrees Celsius by evaluating  $D_{out} = A \cdot \mu_T + B$ , where  $A$  ( $\sim 610$ ), and  $B$  ( $\sim -283$ ) are also calibration parameters.

The coefficients  $A$ ,  $B$  and  $\alpha$  can be found by batch-calibration, which involves calibrating several TDC samples over the desired temperature range. Due to the PTAT spread of  $V_{BE}$ , however, the resulting inaccuracy of individual samples will still be in the order of several degrees. To obtain higher accuracy,  $V_{BE}$  must be individually trimmed.

Conventionally, the information required to trim  $V_{BE}$  is determined by temperature calibration. This involves placing the TDC in good thermal contact with a reference temperature sensor. After thermal equilibrium is reached, the die temperature  $T_{die}$  is known (assuming negligible self-heating) and the output of each sample can then be corrected by applying a PTAT trim to  $V_{BE}$  [15]. Reaching thermal equilibrium, however, is a slow (minute-long) process, which significantly increases the TDC's production costs.

Although high accuracy (less than 0.1°C over the military temperature range) can be achieved after the 1-point calibration of ceramic-packaged samples, 2-point calibration is required to correct for the non-PTAT errors caused by the packaging stress present in plastic-packaged samples [10],

[11]. In other words, the calibration parameters  $A$  and  $B$  must be adjusted to preserve accuracy [10], [11]. However, the costs associated with 2-point calibration are quite high, especially for packaged devices.

### C. Voltage calibration

Voltage calibration (VCAL) does not require an accurate temperature reference, and is thus a faster alternative to temperature calibration [16], [17]. Instead,  $T_{die}$  is determined by comparing  $\Delta V_{BE}$  to an external voltage reference  $V_{ext}$ . Experiments show that  $\Delta V_{BE}$  is quite robust to process variations [14] and to the mechanical stress caused by the plastic packaging [10].

VCAL involves two steps. First, the TDC digitizes the ratio  $X_V = V_{ext}/\Delta V_{BE}$ , from which  $T_{die}$  can be estimated with the help of a master curve obtained by a one-time batch-calibration. Second, the TDC digitizes the ratio  $X_T = V_{BE}/\Delta V_{BE}$ , which corresponds to an untrimmed temperature output. Since both steps are completed in quick succession (within a few hundred milliseconds),  $T_{die}$  can be assumed to be constant. The output of the TDC can then be corrected by trimming  $V_{BE}$ .

The accuracy of VCAL relies on the accuracy of  $V_{ext}$  and  $\Delta V_{BE}$ . While  $V_{ext}$  is an external voltage, which can be quite accurately defined, ensuring the accuracy of  $\Delta V_{BE}$  is more challenging. For two PNPs biased via their emitters

$$\Delta V_{BE} \approx \eta \cdot kT/q \cdot \log(p) + \eta \cdot kT/q \cdot \Delta\beta/\beta^2 + r_s \cdot (p-1) \cdot I_b \quad (1)$$

Where  $\eta$  is the non-ideality factor of the PNPs,  $r_s$  is their equivalent series resistance,  $\beta$  is their nominal current gain,  $\Delta\beta$  is the difference in  $\beta$  at the two emitter currents,  $p$  is the emitter current ratio, and  $I_b$  is the bias current. In this design, the use of low bias current ( $I_b \approx 160$  nA at 25°C), and DEM to establish the 1 : 5 ratio are enough to ensure that the equivalent spread in  $\Delta V_{BE}$  is less than  $\pm 0.15^\circ\text{C}$  over different batches [14] and packages [10].

## III. HEATER-ASSISTED VOLTAGE CALIBRATION

### A. Principle of operation

Since  $\Delta V_{BE}$  can be used to accurately estimate  $T_{die}$ , VCAL can be carried out at any temperature. The only requirement is that  $T_{die}$  is stable during its two steps. HA-VCAL exploits these features, by using an on-chip heater to rapidly warm up the die to an elevated, but not very well-defined, temperature (see Fig. 2). VCAL can then be carried out at two temperatures: at room temperature ( $T_1$ ), and at this elevated temperature ( $T_2$ ).

Initially, the heater is off, and  $T_{die} = T_1$ . The TDC then outputs  $T_{1V}$ , and  $T_{1T}$ , where  $T_{1V}$  is the estimated die temperature obtained from  $X_V = V_{ext}/\Delta V_{BE}$ , and  $T_{1T}$  is the untrimmed output temperature derived from  $X_T = V_{BE}/\Delta V_{BE}$ . This set of values ( $T_{1T}$ ,  $T_{1V}$ ) is similar to that obtained during conventional VCAL. The heater is then turned on, thus elevating  $T_{die}$  to  $T_2$ , after which the TDC outputs  $T_{2V}$ , and  $T_{2T}$ . The two sets of values ( $T_{1V}$ ,  $T_{1T}$ ), ( $T_{2V}$ ,  $T_{2T}$ ) can then be used to perform a 2-point calibration.

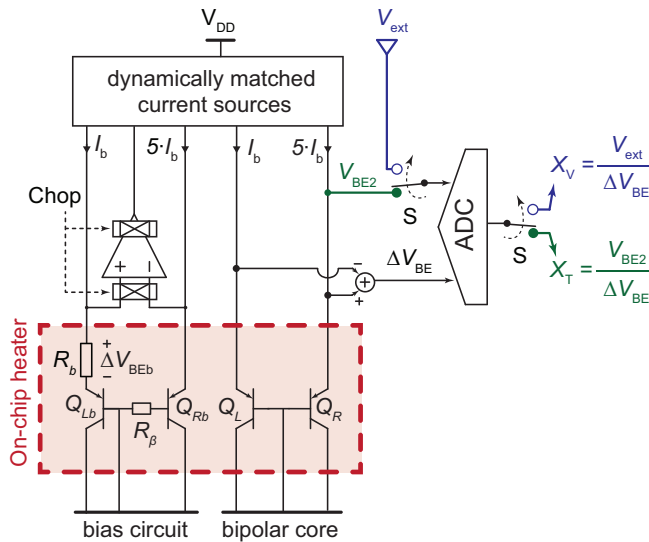


Fig. 2. Heater-assisted voltage calibration. The on-chip heater heats up the temperature-sensitive elements, and VCAL is repeated at two temperatures, room-temperature and an elevated temperature.

Due to the thermal time-constants of the die and package, the transient in  $T_{die}$  caused by turning on the heater takes several minutes to fully settle (see Fig. 3, top). Rather than waiting for this, a 1<sup>st</sup> order interpolation scheme is used to ensure that  $T_{die}$  is effectively the same during both steps of VCAL. This involves averaging the value of  $T_V$  before ( $T_{VB}$ ), and after ( $T_{VA}$ ), the  $T_T$  conversion (see Fig. 3, top). For consistency, this is done during both phases of HA-VCAL.

Fig. 3, bottom, shows the difference between the measured  $T_V$  and its interpolated value  $0.5 \cdot (T_{VA} + T_{VB})$  during a heating transient. It can be seen that the error after interpolation reaches the noise-level in less than 0.5 s, even as the die-temperature changes from  $\sim 25^\circ\text{C}$  to  $\sim 90^\circ\text{C}$ . HA-VCAL, therefore, can be reliably carried out in less than a second.

### B. On-chip heater

In order to perform the HA-VCAL, it is sufficient to heat just the temperature-sensitive elements of the TDC: the four PNPs ( $Q_R$ ,  $Q_L$ ,  $Q_{Rb}$  and  $Q_{Lb}$ ) and the two poly-resistors ( $R_b$  and  $R_\beta$ ). As a result, the required heater can be quite small, saving both power and area. To be as close as possible to the PNPs and the poly resistors, the heater is realized in Metal-2 (Fig. 4, top), with Metal-1 being reserved for local routing.

In [18], four on-chip heaters were used to calibrate a frequency reference. To minimize on-chip temperature gradients, the heaters were placed far away from the circuits being calibrated, and a heat-spreading metal layer was applied to the bottom of the die during a post-fabrication step. In this work, instead of attempting to heat the die uniformly, a single heater is used to create a hot-spot directly above the circuit to be calibrated. As a result, only a small volume of silicon needs to be heated, resulting in much faster calibration and obviating the need for an additional heat-spreading metal layer.

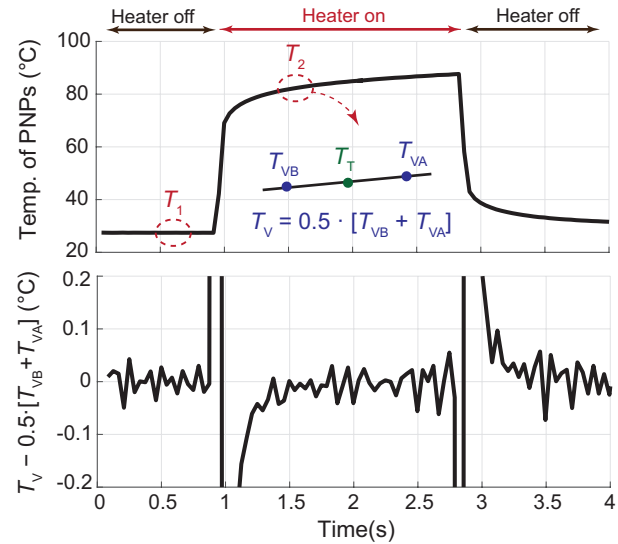


Fig. 3. Measured die temperature taken from [10]. (Top) temperature of PNPs, when the on-chip heater is pulsed. (Bottom) measured interpolation error.

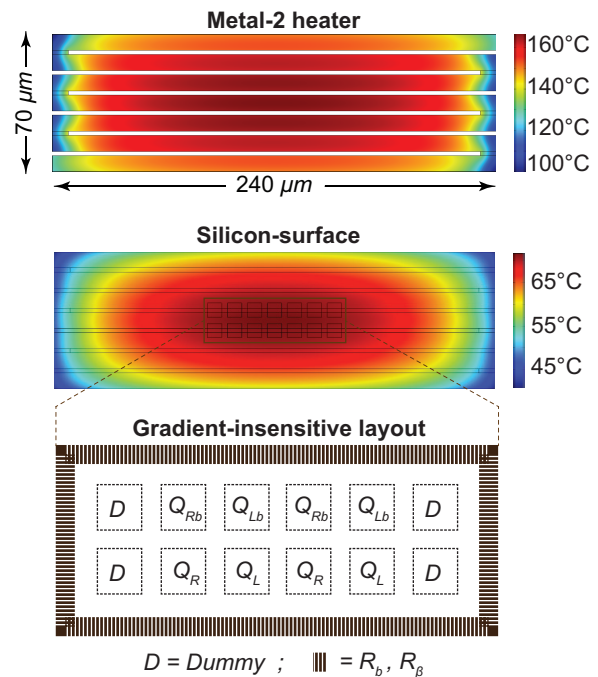


Fig. 4. (Top) serpentine-shaped Metal-2 heater, and the simulated temperature gradient using COMSOL. (Middle) temperature gradient on the silicon surface under the heater. (Bottom) gradient-insensitive layout.

However, without any special measures, large temperature gradients will be created under the heater. These could cause significant temperature differences between  $Q_L$  and  $Q_R$ , causing errors in  $\Delta V_{BE}$ , and thus errors in both  $T_{2V}$  and  $T_{2T}$ . Similarly, temperature difference between the poly resistors and the PNPs, or between  $Q_{Lb}$ , and  $Q_{Rb}$  could cause errors in the bias current, and thus errors in  $V_{BE}$ , and, finally, errors in  $T_{2T}$ . Temperature differences between the PNPs of the bias

circuit, and the bipolar core could also cause errors in the  $\beta$ -compensation, again causing errors in  $V_{BE}$ , and hence in  $T_{2T}$ .

Fig. 4 shows the results of a COMSOL simulation of a serpentine heater in Metal-2 that dissipates 0.5 W. Large temperature gradients can be seen in the heater and on the silicon substrate under the heater. There is also a significant vertical gradient between the heater and the silicon substrate.

To mitigate the effect of such gradients, the sensitive elements of the TDC are placed in a small (0.002 mm<sup>2</sup>) area under the much larger heater (0.017 mm<sup>2</sup>). In addition, a gradient-insensitive layout is used (Fig. 4, bottom). Each PNP is split into two halves and placed in a common-centroid manner around the heater's symmetry axes (Fig. 4, bottom). Similarly, all top-level metal routing above the heater was done symmetrically with respect to its axes of symmetry.

The resistors  $R_b$  and  $R_\beta$  are located around the PNPs, and are thus further away from the heaters centroid. Being implemented in Poly, however, they are actually closer to the Metal-2 heater than the PNPs. These two effects partially counter-act each other and help reduce the temperature difference between the PNPs and the resistors. Simulations show that their average temperature difference is  $\sim 7^\circ\text{C}$ . Given the low temperature-coefficient of the resistors, this results in a 0.2% error in their resistance, which corresponds to a negligible error of 45 m $^\circ\text{C}$  in  $T_{2T}$ .

### C. Local heating versus uniform heating

In normal operation, the TDC is uniformly heated by changes in ambient temperature. During HA-VCAL, however, it is heated locally. In this case, the area directly under the heater will be significantly hotter than the rest of the TDC, i.e. the front-end and the ADC. To prevent calibration errors, the performance of this circuitry should be the same during both modes of operation.

Temperature-dependent errors in the front-end, such as opamp offset and current ratio mismatch, are mitigated by the use of chopping and DEM. Similarly, ADC errors, such as offset and gain-error, are mitigated by the use of correlated-double sampling, system-level chopping, and DEM. These techniques make the front-end and the ADC insensitive to temperature gradients. As a result, their performance is essentially the same during both local and uniform heating.

However, the leakage current of the ADC's sampling switches increases exponentially with temperature. Compared to normal operation, the temperature gradients created with HA-VCAL will then cause different levels of leakage current, which could be a potential source of calibration errors.

One way to avoid such errors is to also place the sampling switches under the heater. However, this would require a significant increase in the area of the uniformly heated zone under the heater, and thus to a significantly larger heater. A better solution is to use circuit techniques to make switch leakage negligible compared to the bias currents of the critical PNPs.

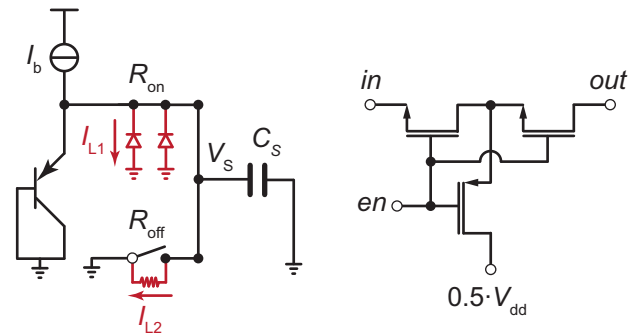


Fig. 5. (Left) switch leakage causes  $V_S$  to be different from  $V_{BE}$ .  $I_{L1}$  flows through the reverse diodes of the switches.  $I_{L2}$  flows through the off-resistance of the switches. (Right) low-leakage switch adapted from [19].

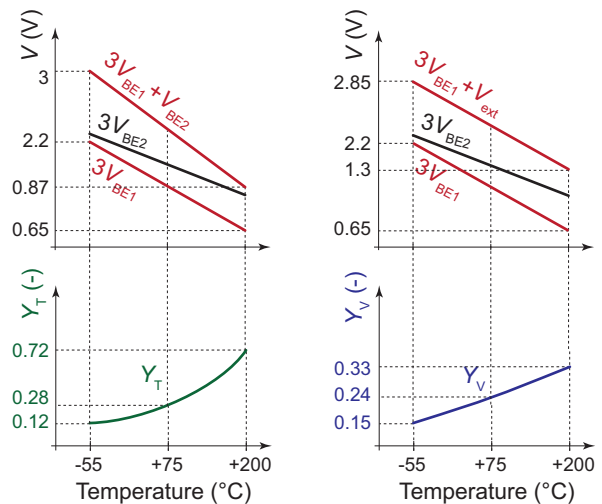


Fig. 6. Charge-balancing scheme in the modulator. The modulator outputs  $Y_T$  in the normal mode, and  $Y_V$  in the VCAL mode.

## IV. LOW-LEAKAGE READ-OUT CIRCUIT

### A. Switch leakage

Fig. 5, left, shows a simplified diagram of the sampling network of the SC-ADC used in the TDC. Switch leakage will alter the PNP's bias current and thus cause errors in  $V_{BE}$ . Furthermore, errors in the sampled voltage  $V_S$  will be caused by leakage current flowing through the on-resistance  $R_{on}$  of the switch. There are two components of leakage current:  $I_{L1}$  and  $I_{L2}$ . The former is associated with the reverse-biased junctions between the substrate and the source and drain of the sampling switch, while the latter is the current that flows through the off-resistance  $R_{off}$  of any other switches connected to  $C_S$ . The sampling error in  $V_S$  due to  $I_{L1}$  is directly proportional to the total number of switches connected to the BJTs. While, the sampling errors due to  $I_{L2}$  are a function of  $R_{on}/(N \cdot R_{off})$ , where  $N$  is the number of "off" switches involved.

In previous work [10], HA-VCAL was applied to a TDC based on a zoom ADC [11]. Its sampling network consisted of a capacitor array with 64 unit elements, each of which could be connected to  $V_{BE1}$ ,  $V_{BE2}$ , or  $V_{ext}$  via three sampling



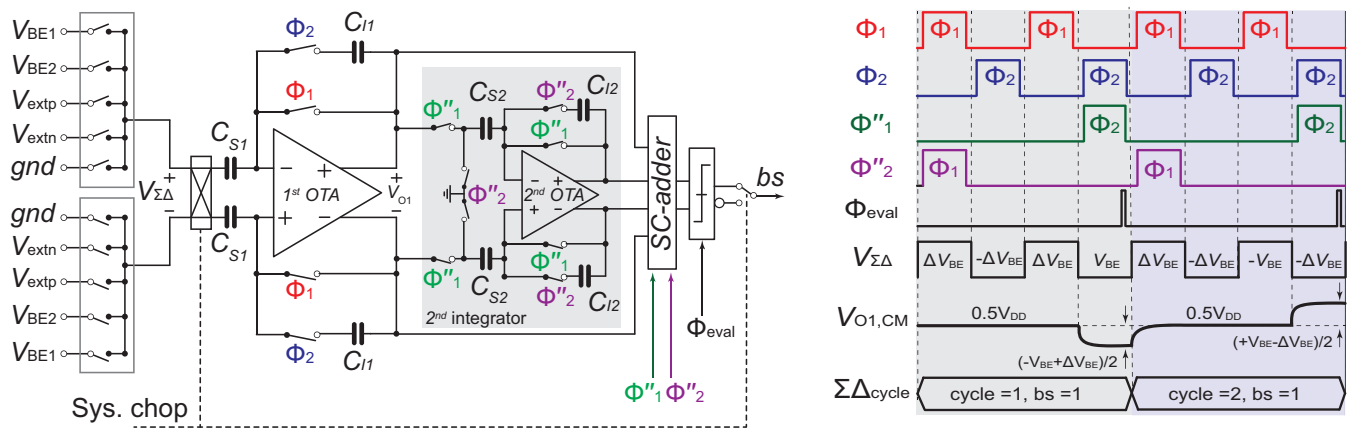


Fig. 7. (Left) the low-leakage ADC. (Right) timing diagram.

switches. The switches enabled the application of DEM to the capacitor array, thus significantly mitigating the effect of capacitor mismatch, but resulting in a total of 192 sampling switches. Their leakage led to a small systematic error after HA-VCAL.

As shown in Fig. 7, the proposed ADC uses only two sampling capacitors, which then require 10 switches to sample  $V_{BE1}$ ,  $V_{BE2}$  and  $Gnd$ , as well as to differentially sample  $V_{ext}$  via  $V_{extn}$  and  $V_{extp}$ . Compared to the 192 switches used in [10], the substantial reduction in the number of switches proportionally reduces the effect of switch leakage. Furthermore, as shown in Fig. 5, right, the effective off-resistance of each switch was increased by adopting a T-configuration [19]. This consists of two NMOSFETs in series with a PMOSFET that biases the central node to  $V_{DD}/2$  when the switch is off. As a result, one of the two NMOSFETs is always in the deep cut-off region. As will be shown in the following sections, the proposed low-leakage ADC enables a higher accuracy at high temperatures, as well as a more robust HA-VCAL.

### B. Charge-balancing scheme in the low-leakage ADC

Using two sampling capacitors in the proposed ADC requires a different charge-balancing scheme than that of the zoom-ADC. Similar to [20], the ADC digitizes the ratio  $Y_T = 3 \cdot \Delta V_{BE} / V_{BE2}$ , which varies from 0.15 to 0.72 as  $T_{die}$  varies from  $-40^\circ\text{C}$  to  $+180^\circ\text{C}$ . The factor of 3 was chosen to maximize the ADC's dynamic range in this temperature range.

In each cycle of the modulator, the 1<sup>st</sup>-stage integrates a charge proportional to  $3 \cdot \Delta V_{BE}$ , when  $bs = 0$ , or a charge proportional to  $3 \cdot (\Delta V_{BE} - V_{BE2})$ , when  $bs = 1$ . This results in the desired decimated value:  $Y_T = 3 \cdot \Delta V_{BE} / V_{BE2}$ . As shown in Fig. 6, this charge-balancing scheme is equivalent to setting the ADC's input to  $3 \cdot V_{BE2}$  and then straddling it with two temperature-dependent references  $3 \cdot V_{BE1}$  and  $3 \cdot V_{BE1} + V_{BE2}$ .

During VCAL,  $V_{BE2}$  is replaced by  $V_{ext}$ . The ADC then outputs  $Y_V = 3 \cdot \Delta V_{BE} / V_{ext}$ , which varies from 0.15 to 0.33 (for  $V_{ext} \sim 0.65\text{ V}$ ) over the operating temperature range. The factor 3 is maintained for simplicity, even though it does not optimize the ADC's dynamic range.

Compared to the previous zoom ADC [10], the proposed low-leakage ADC requires much simpler control logic, as the modulator is not preceded by a SAR conversion. Also, since the same capacitors sample  $\Delta V_{BE}$  and  $V_{BE}$ , there is no need for DEM, and the associated logic. However, the maximum loop-filter input is now  $3 \cdot (\Delta V_{BE} - V_{BE2})$ , which is much larger than the  $2 \cdot \Delta V_{BE}$  of the zoom-ADC [11]. In order to handle this extra swing with the same current-reuse OTAs used in [14], the 1<sup>st</sup> integrator's capacitor was simply increased, to  $710\text{ fF}$ , i.e. by about  $4\times$ .

### C. Sampling scheme in the low-leakage ADC

In order to implement the gain factor (3) required by the charge-balancing scheme, the low-leakage ADC samples  $\Delta V_{BE}$ ,  $V_{BE}$ , or  $V_{ext}$  multiple times. As shown in Fig. 7, right, the 1<sup>st</sup> integrator uses 4 non-overlapping clock phases  $\phi_1$ , and  $\phi_2$  to sample and transfer the required charge to the integration capacitor  $C_{I1}$ . During the 4<sup>th</sup> phase, the output voltage of the 1<sup>st</sup>-stage is sampled by the 2<sup>nd</sup>-stage integrator during  $\phi''_1$ , and then accumulated during  $\phi''_2$  to realize a one-cycle integration delay. The output voltages of the two stages are then summed by an SC-adder and evaluated by the comparator (triggered by  $\phi_{eval}$ ) to generate the output bitstream  $bs$ . The sampling capacitor  $C_{S1}$  is  $125\text{ fF}$ , and each sampling phase takes  $1.25\ \mu\text{s}$ , resulting in a  $5\ \mu\text{s}$   $\Sigma\Delta$  cycle.

The differential input voltage  $V_{\Sigma\Delta}$  of the modulator is shown in Fig. 7, right, for the case when  $bs = 1$ . The input switches then realize the charge-balancing scheme by applying the following sequence of voltages to  $V_{\Sigma\Delta}$ :  $+\Delta V_{BE}$ ,  $-\Delta V_{BE}$ ,  $+\Delta V_{BE}$ ,  $+V_{BE}$ . This sequence, however, also has a CM component equal to  $(V_{BE} + \Delta V_{BE})/2$ , which will also be integrated. Although this component will initially be suppressed by the integrators CMFB circuit, it is cumulative and may eventually cause the 1<sup>st</sup> OTA to clip.

To prevent this, as in [21], the CM component is inverted each time the  $bs = 1$  state occurs. This involves applying toggling between the  $V_{\Sigma\Delta}$  sequence described above and the following sequence:  $+\Delta V_{BE}$ ,  $-\Delta V_{BE}$ ,  $-V_{BE2}$ ,  $+\Delta V_{BE}$ . This results in the same differential voltage, but inverts its CM



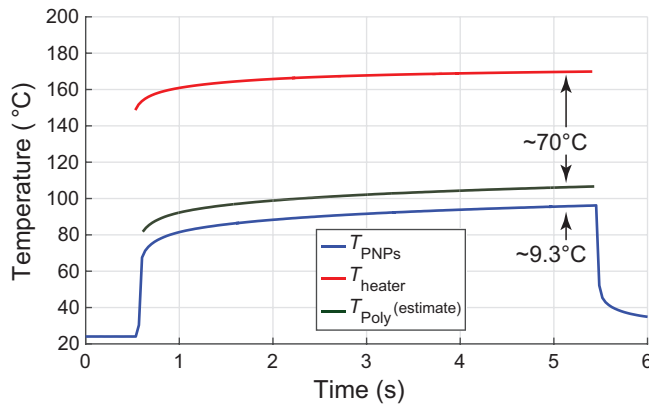


Fig. 11. Measured temperature of the PNPs, and the on-chip heater, in a thermal transient.

2<sup>nd</sup>-stage integrators, and the comparator consume 21%, 14%, and 8%, respectively. For flexibility, the calibration logic, and decimation filter are realized off-chip. The TDC achieves a thermal-noise limited resolution of 23 *mk* (*rms*), in a 20 *ms* conversion time. This corresponds to a resolution *FoM* of 103 *pJK*<sup>2</sup>.

To evaluate the TDC's accuracy, 24 samples from one wafer were packaged in ceramic (DIL-28) and then characterized from  $-40^{\circ}\text{C}$  to  $+180^{\circ}\text{C}$  in a climate chamber. As shown in Fig. 10, top, the TDC achieves  $\pm 0.45^{\circ}\text{C}$  ( $3\sigma$ ) inaccuracy after batch-calibration. This improves to  $\pm 0.2^{\circ}\text{C}$  (Fig. 10, bottom) after temperature calibration at room-temperature followed by a PTAT trim. Note that no systematic non-linearity correction is applied.

Table I summarizes the TDC's main characteristics and compares it with [3], [10], which are both based on zoom-ADCs, and other high-temperature CMOS TDCs. Although not as energy efficient as the zoom ADC based designs, its relative inaccuracy is comparable to [10] and  $2\times$  better than [3]. With the exception of [10], it also consumes significantly less power than the other designs.

#### A. Heater operation

Since the resistance of the heater has a significant TC ( $\sim 0.3\%/^{\circ}\text{C}$ ), the temperature of the heater can be accurately determined by measuring its resistance. This was calibrated in a climate chamber, and found to vary from about  $18\Omega$  at  $25^{\circ}\text{C}$  to about  $27\Omega$  at  $180^{\circ}\text{C}$ . On-chip Kelvin contacts were used to exclude the series resistances introduced by the bonding wires, PCB traces and external switches. Similarly,  $\Delta V_{BE}$  was voltage calibrated to determine the exact temperature of the PNPs.

Fig. 11 shows the measured response of the PNPs and the heater when a 5.3 V pulse is applied to the heater. Both the heater and the TDC are clocked by an FPGA, allowing their operation to be accurately synchronized. Initially, the temperature of the heater rapidly rises from  $\sim 25^{\circ}\text{C}$  to  $\sim 170^{\circ}\text{C}$ . The temperature of the PNPs also changes rapidly, but only reaches a maximum of  $\sim 90^{\circ}\text{C}$ , since they are separated from the heater by insulating layers of oxide. The initial rapid rise

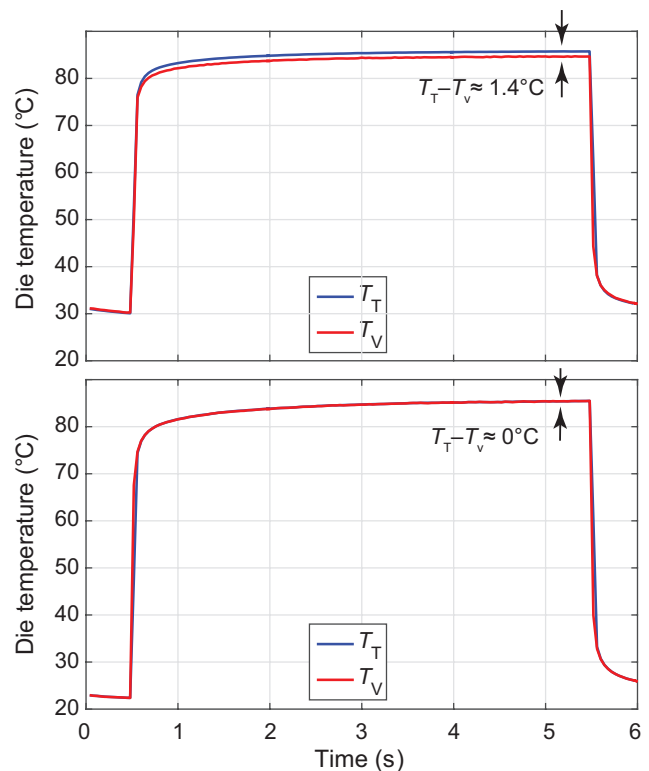


Fig. 12. Voltage calibrated  $T_V$  and temperature calibrated  $T_T$  outputs of TDCs during a transient heating. (Top) based on a zoom ADC, (bottom) based on the proposed low-leakage ADC.

in temperature is followed by a slow settling phase, which is mainly due to the large thermal time-constant of the package.

The temperature difference between the poly resistors and the PNPs can be estimated by assuming that the temperature difference ( $\sim 80^{\circ}\text{C}$ ) between the PNPs and the heater is uniformly distributed over the oxide layers between them. Using the layer thicknesses given in the technology datasheet, the estimated poly-PNP temperature difference is  $\sim 9.3^{\circ}\text{C}$ , in reasonable agreement with the COMSOL simulations.

#### B. Local heating versus uniform heating

An experiment was carried out to verify that the output of the TDC during local heating is well correlated to its output during uniform heating. In other words, to verify that local heating no longer causes the systematic calibration error observed in [10]. First, both temperature calibration and voltage calibration were performed on a TDC while it was uniformly heated in a climate chamber. The resulting outputs,  $T_T$  and  $T_V$ , respectively, were then used to obtain master curves. These curves were then used to determine the temperature of the TDC during HA-VCAL. As shown in Fig. 12, bottom, there is excellent agreement between the two curves (mainly limited by the TDCs own noise). In contrast, a systematic error of about  $1.4^{\circ}\text{C}$  can be seen in the results obtained with the TDC of [10]. This demonstrates the effectiveness of the proposed ADC in mitigating front-end errors due to switch leakage.



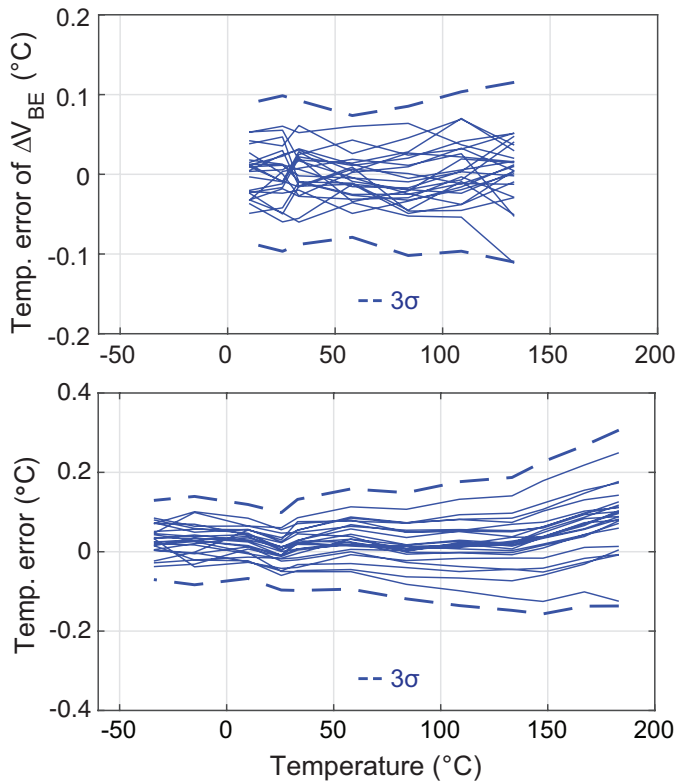


Fig. 13. TDC inaccuracy using conventional voltage calibration. (Top) inaccuracy of  $T_V$  obtained from  $\Delta V_{BE}$  measurement. (Bottom) voltage calibration at room-temperature.

### C. Conventional VCAL versus HA-VCAL

The ultimate accuracy of HA-VCAL is limited by the spread in  $T_V$  above room temperature. Fig. 13, top, shows the spread in  $T_V$  from 10°C to 130°C. As shown in Fig. 13, bottom, after VCAL at  $\sim 25^\circ\text{C}$ , the TDC achieves  $\pm 0.3^\circ\text{C}$  ( $3\sigma$ ) inaccuracy from  $-40^\circ\text{C}$  to  $+180^\circ\text{C}$ . This improves to  $\pm 0.25^\circ\text{C}$  after HA-VCAL at  $T_1 \sim 25^\circ\text{C}$  and  $T_2 \sim 110^\circ\text{C}$ , as shown in Fig. 14, top. Further increases in  $T_2$ , which would be expected to result in even higher accuracy, were limited by the heater's maximum current-handling capability.

To further verify the robustness of HA-VCAL, 2-point VCAL was performed by uniformly heating the same TDC samples in a climate chamber. Fig. 14, bottom, shows the results, where  $T_1$  and  $T_2$  are the same as in Fig. 14, top. This results in an inaccuracy of  $\pm 0.2^\circ\text{C}$  ( $3\sigma$ ), which is slightly better than those obtained with HA-VCAL. However, this comes at the expense of significantly more calibration time: tens of minutes versus 0.5 s for HA-VACL.

### D. Post package HA-VCAL

HA-VCAL can also be used to correct for the non-PTAT shift in  $V_{BE}$  caused by packaging stress [23]–[25]. This shift depends on the location of the sensing PNPs on the die, as well as on the package type and size. For a given package, this can be mitigated with the help of package-specific calibration parameters, obtained by batch-calibration. Higher accuracy can be achieved with 2-point temperature

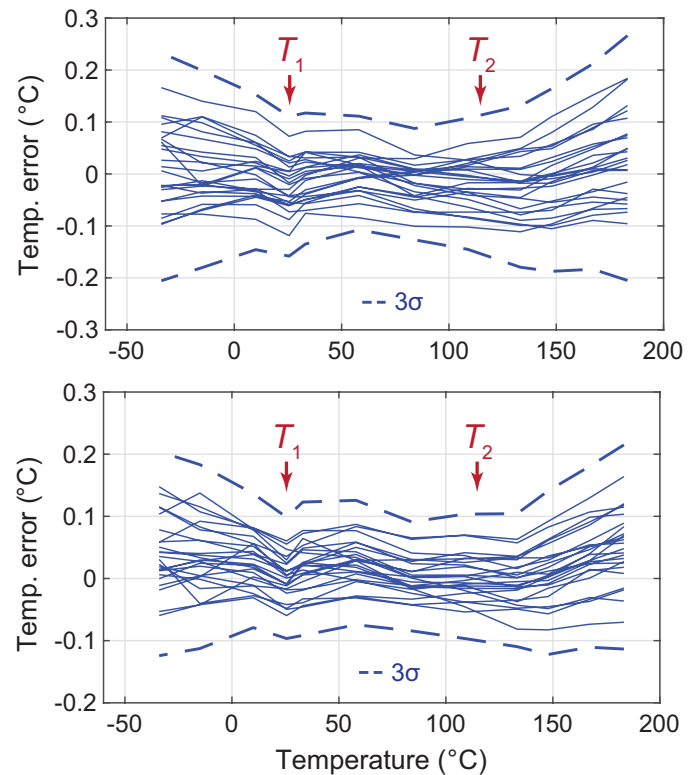


Fig. 14. TDCs inaccuracy after using heater-assisted 2-point voltage calibration. (Top) using the on-chip heater. (Bottom) using a climate chamber.

calibration, at the expense of increased cost. HA-VCAL is a low-cost alternative, since it can be applied to any package and does not require a temperature-controlled environment. This has been demonstrated in [10], where HA-VCAL was used to obtain similar accuracy in both plastic (SO-20) and ceramic packaged (DIL-20) TDCs.

## VI. CONCLUSION

A TDC that operates up to  $+180^\circ\text{C}$ , while achieving state-of-the-art inaccuracy ( $\pm 0.2^\circ\text{C}$  ( $3\sigma$ ), 24 samples) and power consumption ( $9.75 \mu\text{W}$ ) has been presented. It employs a SC-ADC based on two sampling capacitors, substantially reducing the number of switches, and hence the associated high-temperature leakage currents in its analog front-end. The TDC is also equipped with an on-chip heater, which is used to implement Heater-Assisted Voltage Calibration. This enables rapid 2-point calibration with purely electrical measurements. Although somewhat less accurate than temperature calibration ( $\pm 0.25^\circ\text{C}$  ( $3\sigma$ )), it is much faster and cost efficient, since it can be carried out within 0.5 s without the need for a temperature-stabilized environment.

## ACKNOWLEDGMENT

The authors would like to thank NXP Semiconductors for chip fabrication, Robert Van Veldhoven, Sha Xia, and Berry Buter for their help and support of this work.

## REFERENCES

- [1] W. J. Fleming, "Overview of automotive sensors," *IEEE Sensors J.*, vol. 1, no. 4, pp. 296–308, Dec 2001.
- [2] R. W. Johnson, J. L. Evans, P. Jacobsen, J. R. Thompson, and M. Christopher, "The changing automotive environment: high-temperature electronics," *IEEE Trans. Electronics Packaging Manufacturing*, vol. 27, no. 3, pp. 164–176, July 2004.
- [3] K. Souiri, K. Souiri, and K. Makinwa, "A 40  $\mu$ W CMOS temperature sensor with an inaccuracy of  $\pm 0.4^\circ\text{C}$  ( $3\sigma$ ) from  $-55^\circ\text{C}$  to  $200^\circ\text{C}$ ," in *Proc. ESSCIRC*, Sep. 2013, pp. 221–224.
- [4] B. Rue and D. Flandre, "A SOI CMOS smart high-temperature sensor," in *IEEE International SOI Conference*, Oct 2007, pp. 111–112.
- [5] J. Pathrose, C. Liu, K. T. C. Chai, and Y. Ping Xu, "A time-domain band-gap temperature sensor in SOI CMOS for high-temperature applications," *IEEE TCAS II: Express Briefs*, vol. 62, no. 5, pp. 436–440, May 2015.
- [6] K. Mizuno, N. Ohta, F. Kitagawa, and H. Nagase, "Analog CMOS integrated circuits for high-temperature operation with leakage current compensation," in *Fourth International High Temperature Electronics Conference (HITEC)*, June 1998, pp. 41–44.
- [7] J. Nilsson, J. Borg, and J. Johansson, "Leakage current compensation for a 450 nW, high-temperature, bandgap temperature sensor," in *22<sup>nd</sup> International Conference Mixed Design of Integrated Circuits Systems (MIXDES)*, June 2015, pp. 343–347.
- [8] C. van Vroonhoven, D. D'Aquino, and K. Makinwa, "A  $\pm 0.4^\circ\text{C}$  ( $3\sigma$ )  $-70^\circ\text{C}$  to  $200^\circ\text{C}$  time-domain temperature sensor based on heat diffusion in Si and SiO<sub>2</sub>," in *IEEE ISSCC Dig. Tech. Papers*, Feb 2012, pp. 204–206.
- [9] S. Pan, Ç. Gürleyük, M. F. Pimenta, and K. A. A. Makinwa, "A 0.12mm<sup>2</sup> wien-bridge temperature sensor with 0.1 $^\circ\text{C}$  ( $3\sigma$ ) inaccuracy from  $-40^\circ\text{C}$  to  $180^\circ\text{C}$ ," in *IEEE ISSCC Dig. Tech. Papers*, Feb 2019, pp. 184–186.
- [10] B. Yousefzadeh and K. A. A. Makinwa, "A BJT-based temperature sensor with a packaging-robust inaccuracy of  $\pm 0.3^\circ\text{C}$  ( $3\sigma$ ) from  $-55^\circ\text{C}$  to  $+125^\circ\text{C}$  after heater-assisted voltage calibration," in *IEEE ISSCC Dig. Tech. Papers*, Feb 2017, pp. 162–163.
- [11] K. Souiri, Y. Chae, and K. A. A. Makinwa, "A CMOS temperature sensor with a voltage-calibrated inaccuracy of  $\pm 0.15^\circ\text{C}$  ( $3\sigma$ ) from  $-55^\circ\text{C}$  to  $125^\circ\text{C}$ ," *IEEE J. Solid-State Circuits*, vol. 48, no. 1, pp. 292–301, Jan 2013.
- [12] M. Pertijs, and J. Huijsing, "Bias circuits," U.S. patent 7,446,598 B2, Nov. 4, 2008.
- [13] M. A. P. Pertijs, K. A. A. Makinwa, and J. H. Huijsing, "A CMOS smart temperature sensor with a  $3\sigma$  inaccuracy of  $\pm 0.1^\circ\text{C}$  from  $-55^\circ\text{C}$  to  $125^\circ\text{C}$ ," *IEEE J. Solid-State Circuits*, vol. 40, no. 12, pp. 2805–2815, Dec 2005.
- [14] B. Yousefzadeh, S. Heidary Shalmany, and K. A. A. Makinwa, "A BJT-based temperature-to-digital converter with  $\pm 60$  mK ( $3\sigma$ ) inaccuracy from  $-55^\circ\text{C}$  to  $125^\circ\text{C}$  in 0.16- $\mu\text{m}$  CMOS," *IEEE J. Solid-State Circuits*, vol. 52, no. 4, pp. 1044–1052, April 2017.
- [15] M. A. P. Pertijs and J. Huijsing, *Precision Temperature Sensors in CMOS Technology*. Dordrecht, The Netherlands: Springer, 2006.
- [16] M. Pertijs, and J. Huijsing, "Digital temperature sensors and calibration thereof," U.S. patent 7,674,035 B2, March. 9, 2010.
- [17] M. A. P. Pertijs, A. L. Aita, K. A. A. Makinwa, and J. H. Huijsing, "Low-cost calibration techniques for smart temperature sensors," *IEEE Sensors J.*, vol. 10, no. 6, pp. 1098–1105, June 2010.
- [18] Y. Satoh, H. Kobayashi, T. Miyaba, and S. Kousai, "A 2.9mW,  $\pm 85$ ppm accuracy reference clock generator based on RC oscillator with on-chip temperature calibration," in *IEEE Symp. VLSI*, June 2014, pp. 1–2.
- [19] K. Ishida, K. Kanda, A. Tamtrakarn, H. Kawaguchi, and T. Sakurai, "Managing leakage in charge-based analog circuits with low- $V_{TH}$  transistors by analog T-switch (AT-switch) and super cut-off CMOS," in *IEEE Symp. VLSI*, June 2005, pp. 122–125.
- [20] Z. Tang, Y. Fang, X. Yu, Z. Shi, and N. Tan, "A CMOS temperature sensor with versatile readout scheme and high accuracy for multi-sensor systems," *IEEE TCAS I: Regular Papers*, vol. 65, no. 11, pp. 3821–3829, Nov 2018.
- [21] F. Sebastiano, L. J. Breems, K. A. A. Makinwa, S. Drago, D. M. W. Leenaerts, and B. Nauta, "A 1.2-V 10- $\mu\text{W}$  NPN-based temperature sensor in 65-nm CMOS with an inaccuracy of  $0.2^\circ\text{C}$  ( $3\sigma$ ) from  $-70^\circ\text{C}$  to  $125^\circ\text{C}$ ," *IEEE J. Solid-State Circuits*, vol. 45, no. 12, pp. 2591–2601, Dec 2010.
- [22] S. Zaliasl, J. C. Salvia, G. C. Hill, L. Chen, K. Joo, R. Palwai, N. Arumugam, M. Phadke, S. Mukherjee, H. Lee, C. Grosjean, P. M. Hagelin, S. Pamarti, T. S. Fiez, K. A. A. Makinwa, A. Partridge, and V. Menon, "A 3 ppm  $1.5 \times 0.8$  mm<sup>2</sup>  $1.0 \mu\text{A}$  32.768 kHz MEMS-based oscillator," *IEEE J. Solid-State Circuits*, vol. 50, no. 1, pp. 291–302, Jan 2015.
- [23] B. Abesingha, G. A. Rincon-Mora, and D. Briggs, "Voltage shift in plastic-packaged bandgap references," *IEEE TCAS II: Analog and Digital Signal Processing*, vol. 49, no. 10, pp. 681–685, Oct 2002.
- [24] G. Ge, C. Zhang, G. Hoogzaad, and K. A. A. Makinwa, "A single-trim CMOS bandgap reference with a  $3\sigma$  inaccuracy of  $\pm 0.15\%$  from  $-40^\circ\text{C}$  to  $125^\circ\text{C}$ ," *IEEE J. Solid-State Circuits*, vol. 46, no. 11, pp. 2693–2701, Nov 2011.
- [25] M. Motz, U. Auserlechner, and M. Holliber, "Compensation of mechanical stress-induced drift of bandgap references with on-chip stress sensor," *IEEE Sensors J.*, vol. 15, no. 9, pp. 5115–5121, Sep. 2015.



**Bahman Yousefzadeh** (S'16–M'19) received the B.Sc. degree from Shahid Chamran University, Ahvaz, Iran, in 2009, and the M.Sc. degree from Sharif University of Technology, Tehran, Iran, in 2011, both in electrical engineering. Since 2013, he has been with TUDelft to pursue his Ph.D., which was in collaboration with NXP Semiconductors with a focus on low-cost CMOS temperature sensors.

Since 2019, he joined NXP Semiconductor, Eindhoven, The Netherlands. His research interests include precision analog circuits, sensor interfaces, and

oversampled data converters.

Mr. Yousefzadeh was a recipient of the Best Student Paper Award at the 2016 Symposium on VLSI circuits, and the 2016 Analog Devices outstanding student designer award. He has served as a Reviewer for the IEEE Journal of Solid-State Circuits, and the IEEE Transactions on Circuits and Systems I and II.



**Kofi A. A. Makinwa** (M'97–SM'05–F'11) received the B.Sc. and M.Sc. degrees from Obafemi Awolowo University, Ife, Nigeria, in 1985 and 1988, respectively, the M.E.E. degree from the Philips International Institute, Eindhoven, The Netherlands, in 1989, and the Ph.D. degree from Delft University of Technology, Delft, The Netherlands, in 2004.

From 1989 to 1999, he was a Research Scientist with Philips Research Laboratories, Eindhoven, The Netherlands, where he worked on interactive displays and digital recording systems. In 1999, he

joined the Delft University of Technology, where he is currently an Antoni van Leeuwenhoek Professor and Head of the Microelectronics Department. His research interests include the design of mixed-signal circuits, sensor interfaces and smart sensors. This has led to 16 books, over 250 technical papers, and over 30 patents.

Dr. Makinwa has been on the program committees of several IEEE conferences, and has served the Solid-State Circuits Society as a distinguished lecturer and as an elected member of its Adcom. He is currently the Analog Subcommittee chair of the ISSCC, a member of the editorial board of the Proceedings of the IEEE and a co-organizer of the Advances in Analog Circuit Design workshop and the Sensor Interfaces Meeting. He is an ISSCC top-10 contributor, and a co-recipient of 15 best paper awards, from the JSSC, ISSCC, VLSI, ESSCIRC and Transducers, among others. He is a member of the Royal Netherlands Academy of Arts and Sciences.